



## Recycled Red Mud–Decorated Porous 3D Graphene for High-Energy Flexible Micro-Supercapacitor

Bhattacharya, G., Fishlock, S., Pritam, A., Roy, S. S., & McLaughlin, J. (2020). Recycled Red Mud–Decorated Porous 3D Graphene for High-Energy Flexible Micro-Supercapacitor. *Advanced Sustainable Systems*, 4(4), 1-9. [1900133]. <https://doi.org/10.1002/adsu.201900133>

[Link to publication record in Ulster University Research Portal](#)

**Published in:**  
Advanced Sustainable Systems

**Publication Status:**  
Published (in print/issue): 01/04/2020

**DOI:**  
[10.1002/adsu.201900133](https://doi.org/10.1002/adsu.201900133)

**Document Version**  
Author Accepted version

**General rights**  
Copyright for the publications made accessible via Ulster University's Research Portal is retained by the author(s) and / or other copyright owners and it is a condition of accessing these publications that users recognise and abide by the legal requirements associated with these rights.

**Take down policy**  
The Research Portal is Ulster University's institutional repository that provides access to Ulster's research outputs. Every effort has been made to ensure that content in the Research Portal does not infringe any person's rights, or applicable UK laws. If you discover content in the Research Portal that you believe breaches copyright or violates any law, please contact [pure-support@ulster.ac.uk](mailto:pure-support@ulster.ac.uk).

This is the accepted version of the following article:

*Bhattacharya, G., Fishlock, S. J., Pritam, A., Sinha, S., McLaughlin, J. A., Recycled Red Mud–Decorated Porous 3D Graphene for High-Energy Flexible Micro-Supercapacitor. Adv. Sustainable Syst. 2020, 4, 1900133. <https://doi.org/10.1002/adsu.201900133>, which has been published in final form at <https://onlinelibrary.wiley.com/doi/abs/10.1002/adsu.201900133> .*

This article may be used for non-commercial purposes in accordance with the Wiley Self-Archiving Policy [<https://authorservices.wiley.com/authorresources/Journal-Authors/licensing/self-archiving.html>].

# Recycled Red Mud Decorated Porous 3D Graphene for High-Energy Flexible Micro-Supercapacitor

Gourav Bhattacharya <sup>a,b,1</sup>, Sam J. Fishlock <sup>a,1</sup>, Anurag Pritam <sup>b</sup>, Susanta Sinha Roy <sup>b,\*</sup> and James A. McLaughlin <sup>a,\*\*</sup>

<sup>a</sup> Nanotechnology and Integrated Bioengineering Centre, School of Engineering, University of Ulster, Newtownabbey, BT37 0QB Northern Ireland, UK

Email: [jad.mclaughlin@ulster.ac.uk](mailto:jad.mclaughlin@ulster.ac.uk)

<sup>b</sup> Department of Physics, School of Natural Sciences, Shiv Nadar University, Gautam Buddha Nagar, 201314 Uttar Pradesh, India

Email [susanta.roy@snu.edu.in](mailto:susanta.roy@snu.edu.in)

<sup>1</sup>These authors contributed equally

## Abstract

Flexible micro-supercapacitors, with high energy and power density, and using materials with a low environmental impact are attractive for next generation energy storage devices. Carbon-based materials are widely used for supercapacitors but can be increased in energy density via combination with metal oxides. Red mud is an iron-oxide rich by-product of aluminium production, which needs to be more widely utilized to reduce its environmental damage. To achieve a flexible micro-supercapacitor device with increased energy density, we have realized a laser-induced graphene (LIG) supercapacitor from a polyimide substrate, decorated with red mud nanoparticles (LIG-RM), employing a solid-state ionic liquid using a mixture of PVDF, [EMI][TFSI] and [EMIM][BF<sub>4</sub>]. The fabricated two-electrode flexible device, in an inter-

digitated planar design, with inkjet-printed silver current collectors, has a high energy of 0.018 mWh/cm<sup>2</sup> at a power of 0.66 mW/ cm<sup>2</sup>, with 81 % of capacitance retained after 4000 cycles and good resistance to bending and flexing. The high energy storage performance, brought about through the combination of graphene and red-mud nanoparticles, which would – if not utilized - be an environmental liability, shows a promising material for future energy storage with low environmental impact.

## **Keywords**

Red mud; Flexible supercapacitor; Recycled nanomaterials; Waste management; Waste to wealth.

## **1. Introduction**

Future electronics require flexible, fast charging and low-cost power sources, with long service life and a low environmental impact <sup>[1]</sup>. Flexible electronics are sought after for body-worn healthcare <sup>[2]</sup> and smart consumer devices <sup>[3]</sup> and supercapacitors <sup>[4]</sup>, which store charges physically at the electrode surface are seen as a promising power source due to their high cyclic stability and power density <sup>[5]</sup>.

Carbon-based materials are widely used in supercapacitors as they possess high surface area and electrical conductivity <sup>[6]</sup> and there are abundant inexpensive sources with low environmental impact, such as biomass refinery waste <sup>[7]</sup>, graphite pencil trace <sup>[8]</sup> and widely-available polymers such as polyimide <sup>[9]</sup>. For example, Lin *et al.* showed that treating polyimide (Kapton) films using a commercial infrared CO<sub>2</sub> laser photothermally converts C—O, C=O and N—C bonds into sp<sup>2</sup> bonded carbon, with 2D graphene sheets randomly stacked along the c-axis <sup>[10]</sup>, termed laser-induced graphene or LIG.

1 Whilst carbon is the most widely used element for supercapacitor electrodes, transition metal-  
2 oxides offer potentially higher energy densities <sup>[11]</sup> as they undergo either ultrafast Faradaic  
3 reactions at the electrode-electrolyte interface (Faradic pseudocapacitive) <sup>[12]</sup> or by ion  
4 intercalation (Intercalation pseudocapacitor). Metal-oxides may suffer, however, from  
5 relatively low electrical conductivity <sup>[13]</sup> and poor cyclic stability <sup>[14]</sup> compared with carbon  
6 materials. Carbon/metal-oxide hybrid electrodes have thus been employed as supercapacitors  
7 which retain high power density whilst increasing the energy density <sup>[15]</sup>. Clerici *et al.* <sup>[16]</sup> coated  
8 polyimide in an MoS<sub>2</sub> dispersion, and then CO<sub>2</sub> laser treated to produce metal-oxide decorated  
9 LIG, increasing specific capacitance from around  $\approx 4$  to  $\approx 13$  mF/cm<sup>2</sup> at a low scan rate  
10 (increasing energy density from  $\approx 0.5$   $\mu$ Wh/cm<sup>2</sup> to  $\approx 4$   $\mu$ Wh/cm<sup>2</sup> and power density from  $\approx 20$   
11  $\mu$ W/cm<sup>2</sup> to  $\approx 160$   $\mu$ W/cm<sup>2</sup>).

12 The route of decorating graphene with metal-oxide nanoparticles is, then, promising in order  
13 to increase the energy and power density <sup>[15a, 17]</sup>. However, many of the commonly used metal-  
14 oxide materials such as ruthenium, manganese, nickel, and cobalt are becoming increasingly  
15 expensive <sup>[18]</sup> and have a high environmental impact due to mining and refining processes <sup>[19]</sup>.  
16 Whilst the use of low cost, waste-based materials with low environmental impact, for carbon  
17 supercapacitor electrodes is very widespread, particularly from waste-derived activated  
18 carbons, as recently comprehensively reviewed by Divyashree *et al.* <sup>[20]</sup>, the number of waste  
19 inorganic sources of metal-oxide pseudocapacitive materials is far smaller, although growing.  
20 For example, Fu *et al.* produced micro-particle based supercapacitor electrodes <sup>[21]</sup> and porous  
21 Fe<sub>2</sub>O<sub>3</sub> micro-rods <sup>[22]</sup> from mill-scale, a waste product from the steel industry.

22 Another common waste, red mud (RM) is an environmentally damaging by-product of bauxite  
23 processing which is a mixture of metal-oxides; predominantly Fe<sub>2</sub>O<sub>3</sub> and also including Al<sub>2</sub>O<sub>3</sub>,  
24 SiO<sub>2</sub>, and Na<sub>2</sub>O, amongst others <sup>[23]</sup>. RM had an annual production in the year 2011 of around

120 million tonnes <sup>[24]</sup> which is increasing and is often stored or dumped on the land <sup>[25]</sup>. RM is hazardous due to its alkalinity <sup>[26]</sup> and in 2010 caused environmental damage after a large spill in Hungary <sup>[27]</sup>. Since RM is a mass-produced waste, there is a pressing need to further utilize this material to help prevent it from entering and further damaging the environment <sup>[28]</sup>. Notable work on the applications of RM mainly focuses on water treatment, including dye <sup>[29]</sup>, lead and chromium <sup>[30]</sup>, fluoride <sup>[31]</sup>, chlorophenols <sup>[32]</sup>, and arsenic removal from water <sup>[33]</sup>, in catalysis <sup>[34]</sup> and also as building materials <sup>[35]</sup>. These applications have shown the potential to help reduce the amount of RM entering the environment but there is still under-utilization, and further applications, to boost the uptake of red mud in useful products, will limit damage to the environment.

In our previous work <sup>[36]</sup>, we have used RM from National Aluminum Company Limited (NALCO), India, and used ball-milling to produce ~30-50 nm diameter RM nanoparticles for use as supercapacitor electrodes. RM nanoparticles yielded a specific capacitance of  $\approx 317 \text{ F g}^{-1}$ , at  $10 \text{ mV s}^{-1}$  scan rate in 6 M aqueous KOH electrolyte, and cyclic stability of  $\approx 97 \%$  after 5000 cycles <sup>[36]</sup>, demonstrating promising capability as supercapacitor electrodes.

Performance of a supercapacitor significantly varies with the choice of electrolyte. Among various electrolytes, ionic liquid has been emerged as a very promising electrolyte for supercapacitor studies <sup>[37]</sup> and particularly, polymer-based gel electrolytes are popular in solid-state micro-supercapacitor owing to the solid nature of electrolytes <sup>[38]</sup>.

In this present work, we present a working prototype of a flexible RM nanoparticle-decorated LIG supercapacitor, employing environmentally benign ionic liquids <sup>[39]</sup>, mixture of [EMIM][BF<sub>4</sub>] and [EMIM][TFSI] (1:3), in a PVDF-HFP gel electrolyte (IL: PVDF:HFP=4:1). The addition of RM increases the energy density and a cyclic stability of  $\approx 80\%$  after 4000

cycles at a current density of  $0.3 \text{ mA cm}^{-2}$  was achieved. The use of RM is particularly promising as it (i) actively recycles harmful waste material from the environment and (ii) is a promising power source for future flexible electronics.

## **2. Results and discussion**

### **2.1. Device Fabrication**

To fabricate a micro-supercapacitor, a  $50 \text{ }\mu\text{m}$  thick polyimide substrate was laminated in waterproof masking film (ArCare 90445) and an interdigitated structure outline was laser cut (VLS 230, Universal laser), and the film peeled off (Figure 1(a)). The exposed polyimide was laser-treated (nominal power  $8.1 \text{ W}$ ), which converts the polyimide into a graphene 3-dimensional forest-like structure and was patterned as two interdigitated electrodes (Figure 1(b)). Separately,  $\sim 30$  to  $50 \text{ nm}$  diameter red-mud nanoparticle solution was prepared at  $15 \text{ mg/ml}$  concentration in deionized water and stirred to ensure the dispersion remained uniform, Figure 1(c). We selected the concentration of  $15 \text{ mg/ml}$  after initially measuring the cyclic voltammetry at varying red mud concentrations (Figure S1 in the supporting information), hereafter LIG-RM is used to refer to the flexible device of LIG decorated with RM at this concentration. The interdigitated electrode was dip-coated in the stirring solution for 15 minutes and dried at  $50 \text{ }^{\circ}\text{C}$ . Silver current collectors were printed over the electrode edges using a Dimatix 2805 Inkjet printer, using silver nanoparticle ink (NPS-J, Harimatec Ink) and annealed at  $180 \text{ }^{\circ}\text{C}$  in an oven for one hour. The ionogel mixture, at  $50 \text{ }^{\circ}\text{C}$  was viscous but dries like a gel, was micro-pipetted over the interdigitated fingers of the micro-supercapacitor. The whole assembly was dried at room temperature. The schematic of the fabrication process is shown in Figure 1(a-d).

### **3.2. TEM and FESEM analysis**

TEM images of RM nanoparticles are represented in Figure S2, here the spherical morphology of the nanoparticles is clear, and an average size of  $49 \text{ nm} \pm 9 \text{ nm}$  (S.D) was measured. In order to visualize the decoration of red mud particles over the LIG nanofibers, FESEM analysis was carried out and is represented in Figure 1e and cross sectional images ( $60^\circ$  tilt angle) are shown in Figure S3(a-b) which helps to demonstrate the 3D porous nature of LIG. Images of pure LIG and LIG-RM show a relatively uniform dispersion of RM nanoparticles over the LIG forest. SEM EDX elemental mapping is represented in Figure S4 to exhibit the presence and homogenous distribution of carbon, iron, oxygen, aluminium, silicon and sodium within the LIG-RM sample. BET analysis (Figure S5), was used to calculate the surface area of LIG-RM as  $120 \text{ m}^2/\text{g}$ .

### 2.3. XPS analysis

X-ray photoelectron spectroscopy was carried out to probe the presence of different elements in the composite assembly as shown in Figure 1(f-h). The survey scan of the red mud embedded LIG structure shows the presence of  $\text{Fe}_2\text{O}_3$  and oxides of aluminium, silicon, sodium and trace amounts of oxides of magnesium, titanium and manganese in agreement with our previous work<sup>[36]</sup> and is also similar to the red mud XPS data taken by Xu *et al.* and Liu *et al.*<sup>[40]</sup> respectively. The high resolution XPS graphs display the C1s and Fe2p spectra, and the presence of both components confirms the formation of the LIG-RM nanocomposite. The presence of  $\text{sp}^2 \text{ C}=\text{C}$ ,  $\text{sp}^3 \text{ C}-\text{C}$ , CO, O-C-O, O-C=O and  $\pi-\pi^*$  in the carbon XPS spectra matches with the previously reported literature on LIG<sup>[41]</sup>. The high conductivity of LIG has been correlated with the presence of high amount of  $\text{sp}^2$  carbon ( $\sim 284.8 \text{ eV}$ ) and minimal residual oxygen functionalities. The high-resolution XPS result for iron showed the presence of the doublet state of  $2\text{p}^{1/2}$  ( $725.8 \text{ eV}$ ) and  $2\text{p}^{3/2}$  ( $712 \text{ eV}$ ) levels which confirms the presence of hematite phase in red mud nanoparticles<sup>[40b]</sup>.



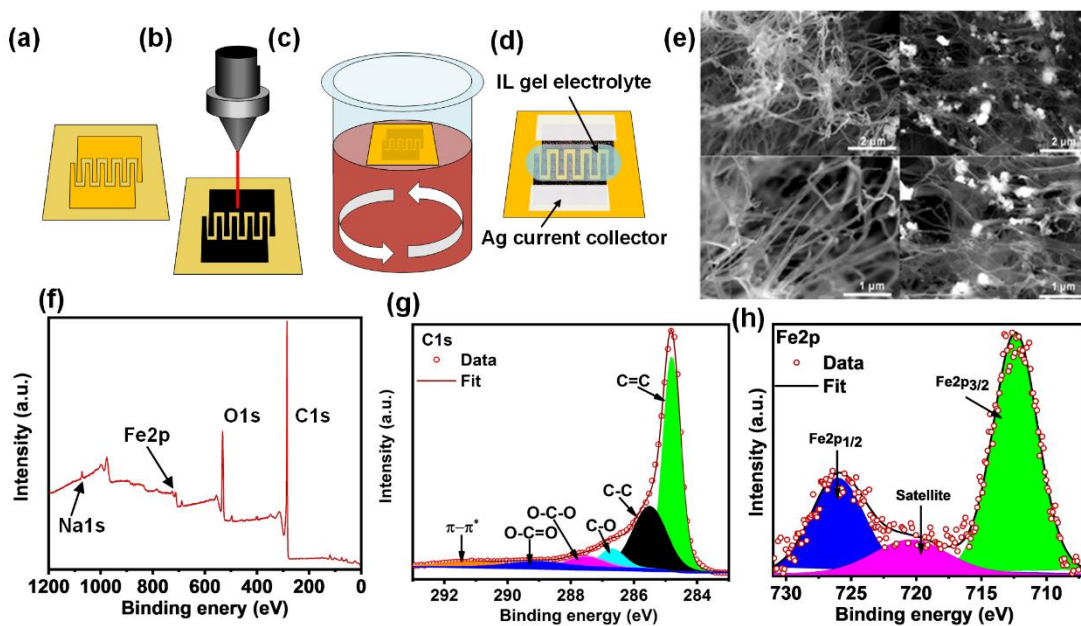


Figure 1. Fabrication of LIG-RM supercapacitor (a) Patterning and peeling of protecting layer (b) Laser-induced graphene formation with CO<sub>2</sub> laser (c) dip-coating in RM solution (d) Silver electrode printing and use of an ionic liquid electrolyte solution; (e) SEM images of pure LIG film (left-hand side) and LIG-RM and XPS spectra of (f) RM decorated LIG, (g) C 1S spectrum of LIG and (h) Fe 2p spectrum of red mud.

## 2.4. Cyclic Voltammetry

The Cyclic voltammogram for a two-electrode symmetric cell assembly for pristine LIG and LIG-RM electrodes in IL mixture electrolyte at a scan rate 20 mVs<sup>-1</sup> is represented in Figure 2(a). From the figure it is quite evident that for the LIG-RM electrode, there is a significant 2-fold improvement in the specific current density as compared to the pristine LIG, along with a higher area under the CV curve.

The variation in the cyclic voltammogram data of LIG-RM sample as a function of scan rate (from 10 to 200 mVs<sup>-1</sup>) is shown in Figure 2(b). The specific cell capacitance,  $C_{cell}$ , is assessed from the CV graphs using equations (1 – 2):<sup>[36]</sup>

$$C_{cell} = 0.5(I/v) \quad (1)$$

where  $I$  is the total current (in Amperes),  $v$  is the scan rate (in Volt/sec). The total current  $I$  can also be obtained from integration of the CV curve as <sup>[36, 42]</sup>.

$$I = \int_{V_i}^{V_f} \frac{i(V)dV}{(V_f - V_i)} \quad (2)$$

where  $V_i$  and  $V_f$  represent the upper and lower bounds of the voltage range. The cell capacitance from  $v = 5$  to 200 mVs<sup>-1</sup> is shown in Figure S6(a). At  $v = 5$  mV s<sup>-1</sup> a cell capacitance of ~18 mF was obtained. At a sweeping potential of 50 mVs<sup>-1</sup>, a cell capacitance of ~ 4 mF was calculated for LIG-RM which is double to that for the pristine LIG device (~ 2 mF).

The specific gravimetric and areal capacitance of the system was also calculated as <sup>[43]</sup>:

$$C_{sg} = 2 \frac{C_{cell}}{m} \quad (3)$$

$$\text{and,} \quad C_{sa} = 2 \frac{C_{cell}}{A} \quad (4)$$

where  $C_{sg}$  is the specific gravimetric capacitance;  $C_{sa}$  is the specific areal capacitance,  $m$  is the active mass and  $A$  is the total device area. The variation of specific areal and gravimetric capacitance as a function of scan rate is represented in Figure 2(c) and Figure S6(b) respectively.

The primary charge storage mechanism of an electrode is governed by the amalgamation of capacitive and intercalation. The appearance of both the processes can be evaluated and

distinguished by monitoring the CV scans at different scan rates rendering to the following power law <sup>[36, 44]</sup>,

$$i = av^b \quad (5)$$

Where  $a$  and  $b$  are adjustable parameters. A value of  $b \approx 1$ , shows a capacitance-dominated current, and  $b$  value of  $\approx 0.5$  shows the current flow at that potential is dominated by diffusion<sup>[45]</sup>.

The  $b$  values between the potentials -1.2 to 1.5 V were obtained for LIG-RM, and the variation of  $b$  with applied potential is plotted in Figure 2(d) with a considerable variation in “ $b$ ” values from 0.3 to 0.85, which suggests that the charge storage mechanism is an amalgamation of both capacitive and diffusion which arises from intercalation/de-intercalation phenomena <sup>[36, 46]</sup>.

As it has been shown that the obtained capacitance is a combination of adsorption and diffusion processes, the next aim was to quantify each element. According to a power-law relationship, when the storage is driven by surface controlled phenomena the current ( $i_{cap}$ ) varies linearly with the scan rate ( $v$ ) <sup>[46a, 47]</sup> and thus

$$i_{cap} = k_1 v \quad (6)$$

where,  $k_1$  is a constant.

If the current is controlled by semi-infinite diffusion, then the current ( $i_{dif}$ ) varies linearly to the square root of scan rate <sup>[46a, 47]</sup>:

$$i_{dif} = k_2 v^{1/2} \quad (7)$$

thus, the total current, <sup>[46a, 47-48]</sup>

$$i_T = i_{cap} + i_{dif} \quad (8)$$

$$= k_1 v + k_2 v^{1/2}$$

$$\therefore \frac{i_T}{v^{1/2}} = k_1 v^{1/2} + k_2 \quad (9)$$

Therefore, the current values at different potential were calculated from CV at different scan rate (200 to 5 mV s<sup>-1</sup>) and then was plotted with  $v^{1/2}$  for different potentials. The plot was linearly fitted and the values of  $k_1$  and  $k_2$  were obtained from the slope and the intercept of the graph respectively [46a]. The contribution of each component may be evaluated from the as-obtained values of  $k_1$  and  $k_2$ . The resultant plots at scan rates 20 mV s<sup>-1</sup> and 100 mV s<sup>-1</sup> where these components are distinguished are shown in Figure S7 and Figure 2(e) respectively.

After deconvolution of the contribution of surface controlled capacitance and intercalation-dominated capacitance, the contributions at different scan rates were plotted in Figure 2(f). The graph exhibits that at lower scan rate the storage is dominated by the intercalation where at a low scan rate of 10 mVs<sup>-1</sup>, only ~ 9% of the capacitance originates from surface adsorption and the rest is intercalation [49]. Correspondingly, at a scan rate of 100 mVs<sup>-1</sup> ~32% capacitance comes from the surface. This is consistent with the fact that at higher scan rate the ions of the electrolyte have less time to intercalate in the electrode assembly [49-50]. The porous nature of the electrode is responsible for intercalation-dominated pseudocapacitive charge storage in the system [51]. The uniform decoration of the RM nanoparticles over 3D hierarchical LIG forest configuration can allow complete exposure of the LIG-RM composite to the ILs [52]. Additionally, the high surface area of LIG provides enhanced contact with both the silver current collector and the IL electrolyte. As a result, the electrolytes can easily penetrate and enhances diffusion domination [53].

Trasatti's method was utilized to differentiate the specific capacitance from either surface or diffusion-driven storage [54] which have different responses to the change in scan rate  $v$  [55]. At

a higher scan rate, the charge is stored at the outer surface since this is more immediately accessible to the electrolyte (the surface may be accessed even at high scan rate). However at lower scan rate, there is a combination of both surface and diffusion-driven storage, since the ions have a longer period to diffuse to the inner electrode surface. Figure S8(a) shows a plot of  $1/C_s$  as a function  $v^{\frac{1}{2}}$  between  $v = 10$  to  $100 \text{ mV s}^{-1}$ , here both storage mechanisms (surface and diffusion-driven) yield a significant contribution <sup>[46a]</sup>. The intercept of this line with best fit of this line  $1/C_s$  was used to calculate the specific capacitance as  $\sim 55.5 \text{ mF cm}^{-2}$  at infinitely slow scan rate. Figure S8(b) shows the graph  $C_s$  as a function of  $v^{-1/2}$  which is used to calculate the surface-controlled capacitance <sup>[55]</sup>. In this graph (S8b), the intercept <sup>[55]</sup> of the plot with the  $C_s$  forecasted the surface controlled capacitance at infinitely high scan rate as  $\sim 4.3 \text{ mF cm}^{-2}$ . The results predict that only  $\sim 8\%$  of the capacitance is surface controlled and  $92\%$  is diffusion-dominated; the dominant mechanism is thus diffusion-dominated pseudocapacitance. The presence of iron oxide and other metal oxides in RM contributes towards the diffusion-driven storage mechanism and the presence of porous LIG backbones enhances the diffusion <sup>[56]</sup>.

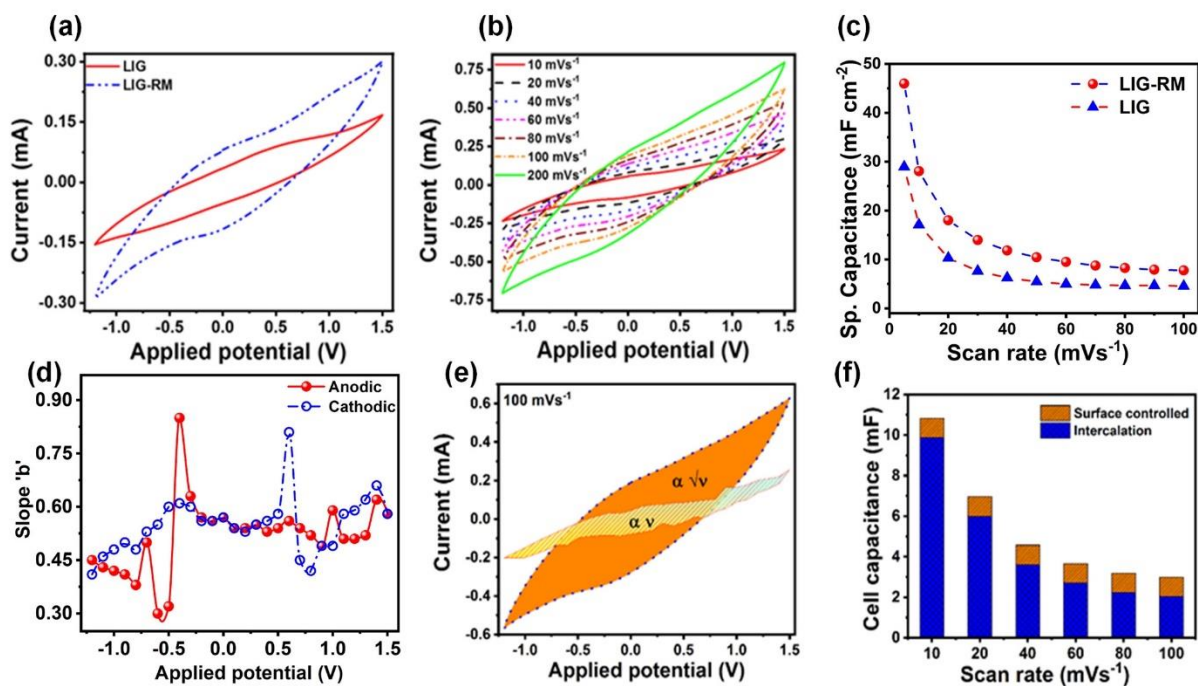


Figure 2. (a) Cyclic voltammogram response of LIG and LIG-RM in IL electrolyte with a scan rate of 20 mV s<sup>-1</sup>, (b) Cyclic voltammogram of LIG-RM in IL electrolyte at different scan rates (c) the variation of specific areal capacitance of the two-electrode LIG-RM supercapacitor (d) “b” (fitting parameter which shows storage mechanism) dependence as a function of applied potential (e) deconvolution of two different storage mechanisms: surface controlled ( $\propto v$ ) and diffusion controlled ( $\propto v^{1/2}$ ) from CV at scan rate 100 mV s<sup>-1</sup> and (f) the contribution of surface controlled and intercalation cell capacitance after deconvolution of the CV graph at different scan rates.

## 2.5. Charging /discharging analysis

To determine the specific capacitance and cyclic stability, the LIG-RM two-electrode symmetric capacitor was galvanostatically charged and discharged between the applied

potential of -1.2 to 1.5 V, in the same ionogel electrolyte. The specific cell capacitance was calculated using <sup>[57]</sup>:

$$C_{cell/CD} = -[i/\{(dV/dt)\}] \quad (10)$$

Where  $C_{cell/CD}$  is the cell capacitance and  $dV/dt$  is average gradient during the discharge cycle. A steady device performance outlined by the quasi-symmetric charging/ discharging cycles. <sup>[58]</sup> whereas the appearance of pseudocapacitance is confirmed from the curvature in the discharge cycle. <sup>[59]</sup>. The charging/discharging plot (at a specific current density of 0.3 mA cm<sup>-2</sup>) for pristine LIG and LIG-RM devices are presented in Figure 3(a). The charge/discharge period in case of the composite device is significantly higher than its pristine counterpart, and consequently shows improved charge storage. The presence of RM nanoparticles not only provide pseudocapacitive contribution and more accessible surface area but also provides a better attachment of electrode-electrolyte assembly which can be attributed towards higher storage in the composite device <sup>[15a]</sup>.

The specific areal capacitance of the electrode material (LIG-RM) ( $C_{sp/elec}$ ) was calculated as <sup>[60]</sup>:

$$C_{sp/elec} = 4 \frac{C_{cell/CD}}{A} \quad (11)$$

where  $A$  is the total device area (77.25 mm<sup>2</sup>).

The areal capacitance was calculated from the charging-discharging graphs for different specific current densities as plotted in Figure 3(b). The maximum areal capacitance of 203 mF cm<sup>-2</sup> was achieved at a specific current density of 0.1 mA cm<sup>-2</sup>, whereas at an extremely high specific current density of 1 mA cm<sup>-2</sup>, a steady capacitance of 15 mF cm<sup>-2</sup> was obtained. The

retention of a moderate capacitance even in such ultra-high specific current density highlights the stability of the cell and supports its suitability as a supercapacitor electrode material.

## 2.6. Long-term cyclic stability

The performance of the supercapacitor in-terms of its stability over long-term cyclic usage was also investigated through the charging/discharging measurement for 4000 cycles at specific current density of  $0.3 \text{ mA cm}^{-2}$ . The capacitance retention as a function of cycle number is plotted in Figure 3(c) and shows ~81 % retention of initial capacitance after 4000 cycles. The retention initially increases to ~110 % of the initial value because of the surface chemical activation of the composite electrode and subsequently better access of the electrolyte ions into the porous LIG assembly during the charging-discharging cycle; a similar behavior has also been reported in the literature <sup>[61]</sup>. The measurements were carried in an ambient atmosphere and without any encapsulation and thus establish the suitability of the two-electrode device as a long-term energy storage module.

The higher charge retention of the device is due to the porous LIG structure created during the laser treatment <sup>[62, 63]</sup> of the polyimide precursor. Mixed ionic liquid brings forth the short-range rearrangement of ions which plays a dominant role in electrolyte dynamics and electrosorption; the different anions of the electrolytes dampens the alternating layer configuration and reduces the excluded volume effect and in turns enhances the electrostatic interaction in the system and improves the electrolyte dynamics and expand the effective potential window (2.7 V) and charge storage capability of the device <sup>[64]</sup>. Favorable cyclic performance has previously been observed in other mixed-metal oxide-based supercapacitors such as mixed-metal hydroxide nanosheets <sup>[52]</sup>, nickel–manganese oxide (NMO) and cobalt–manganese oxide <sup>[65]</sup> and mixed



V<sub>2</sub>O<sub>5</sub>–TiO<sub>2</sub> supercapacitor electrodes.<sup>[66]</sup> Additionally, the IL and ionogel electrolytes interlock with the porous electrode and minimize material leaching and also improves the robustness of the flexible device<sup>[67]</sup>. The direct inkjet printing of silver current collector on top the LIG-RM assembly provides better attachment and efficient contact for fast charge transport and current collection<sup>[68]</sup>.

## 2.7. Energy and power density

Energy and power densities are the two most fundamental parameters of any energy storage devices. The specific energy density  $E_{elec}$  (mW h cm<sup>-2</sup>) of an electrode in a 2-electrode cell configuration can be calculated as<sup>[43b]</sup>:

$$E_{elec} = \frac{1}{8} C_{cd/cell} V^2 \quad (12)$$

Where the cell capacitance and the effective potential windows are represented by  $C_{cell/CD}$  and  $V$ , respectively. The specific power density  $P_{elec}$  (mW cm<sup>-2</sup>) was calculated using the following equation<sup>[57]</sup>:

$$P_{elec} = E_{elec} / t_d \quad (13)$$

where,  $E_{elec}$  is the specific energy density of the electrode and  $t_d$  is the discharge time.

Performance of the LIG-RM electrodes is presented in a Ragone plot (Power density vs. Energy density) as shown in Figure 3(d). It exhibited the highest energy density of ~51 μWh/cm<sup>2</sup> of energy density at a power density of 0.14 mW/cm<sup>2</sup> (specific current density 0.1 mA cm<sup>-2</sup>) and retained an energy density of ~2 μWh/cm<sup>2</sup> at a very high power density of 1.36 mW/cm<sup>2</sup> (current density of 1 mA cm<sup>-2</sup>), which indicates better stability of the electrode at high current

density. In order to compare the performance of different similar flexible supercapacitors, a comparative Ragone plot was drawn. The performance of LIG-RM was compared with highly stretchable supercapacitors enabled by interwoven CNTs <sup>[69]</sup>, coiled fibrous CNT-MnO<sub>2</sub>-polymer solid-state supercapacitors <sup>[70]</sup>, porous LIG films from polymers <sup>[71]</sup>, in-situ MoS<sub>2</sub> decorated flexible LIG electrodes <sup>[16]</sup>. Though the energy density was very high for the interwoven CNT electrode its power density was very poor <sup>[69]</sup>. On the other hand in spite of having very high power density porous LIG film on polyimide substrate lacks in terms of low energy density.<sup>[71]</sup> Energy and power densities of the MoS<sub>2</sub> decorated LIG <sup>[16]</sup> and coiled CNT-MnO<sub>2</sub>-polymer electrodes <sup>[70]</sup> falls in between and suitable for a high-performance flexible device. Our result in terms of both power and current densities is better in comparison to these two electrodes, which further confirms the suitability of our device as an effective storage device. In our device higher energy density was achieved without sacrificing its inherent higher power density.

## 2.8. Electrochemical impedance analysis

The nature of charge transfer kinetics and ionic diffusions have been probed using Electrochemical impedance spectroscopy (EIS). <sup>[72]</sup>. During the EIS measurement a 10 mV AC perturbation of between applied frequencies 0.1–100 kHz. The Nyquist plots of pristine LIG and LIG-RM samples in IL composite electrolytes are represented in Figure S9. The charge transfer resistance can be qualitatively evaluated by the semicircular diameter of the Nyquist plot. <sup>[57, 73]</sup>. The reduction in the charge transfer resistance of the composite electrode indicates a favorable diffusion of the electrolyte in the LIG-RM surface <sup>[73]</sup>.

The EIS spectra of the prototype device were measured and the EIS data was fitted using a model equivalent circuit and is represented in Figure 3(e). The equivalent circuit consists of a series resistance which is in series with a Warburg impedance. These circuit components are in series with two parallel circuits (in series with each other). The parallel circuit consists of a charge transfer resistance and a constant phase element (CPE) <sup>[74]</sup>. All the parameters obtained from the circuit fitting is represented in Table S1 in the supporting information. The as-obtained series and charge transfer resistances of the solid-state supercapacitor device are similar to that of the impedances recorded for similar supercapacitor devices <sup>[16]</sup>. The presence of Warburg impedance and CPE validates the coexistence of capacitive and diffusion controlled charge storage processes which is in agreement with the diffusion-dominated pseudocapacitive charge storage mechanism.<sup>[36]</sup>

## 2.9. Bending test and flexible prototype device testing

In order to prove the suitability of the flexible device, a bending test was carried out. The prototype device was bent to an arbitrary angle (Figure S10) and the cyclic voltammogram was recorded at a scan rate of 20 mVs<sup>-1</sup>. It is evident that the shape of the CV graph remains almost intact after the bending, Figure S10 inset. The cell capacitance before bending was calculated as ~4.4 mF and after the bending, the value was also found to be ~4.8 mF. The change is minimal, and the results also indicate the acceptance and reliability of the flexible device <sup>[75]</sup>.

Finally, to demonstrate the real-time application of the fabricated flexible device, the glowing of the white LED experiment was performed (Figure 3(f)). Three prototype cells were printed in series and charged using ~7 V using a constant voltage source. After charging the device was connected to a white LED which requires 3.5 V for illumination. The prototype device was

able to power up the LED and a bright illumination was achieved, which demonstrates the successful fabrication of a prototype device.

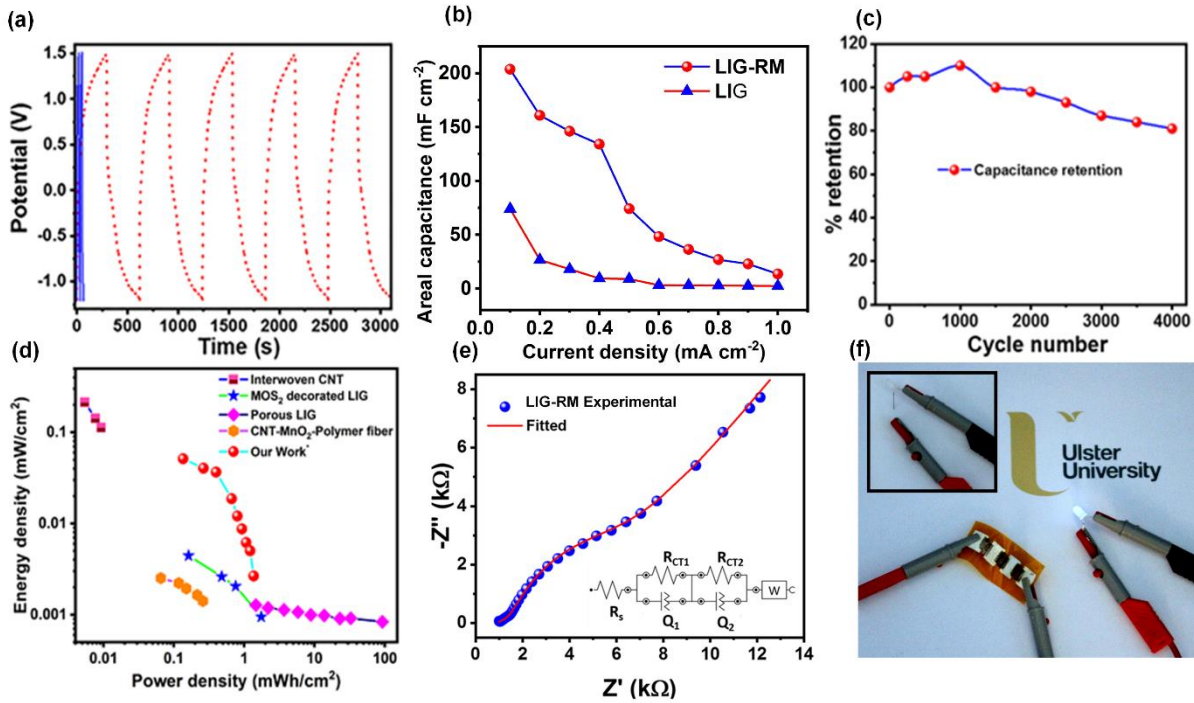


Figure 3. (a) Galvanostatic charging/discharging curve of pristine LIG (solid blue) and LIG-RM (dotted red) at a specific current density of  $0.3 \text{ mA cm}^{-2}$ , (b) variation of specific capacitance with specific current for LIG-RM, (c) the cycling performance of LIG-RM at a specific current density of  $0.3 \text{ mA cm}^{-2}$  for 4000 cycle, (d) Ragone plot related to energy and power density of the LIG-RM supercapacitor device, 2.7 V operation window in comparison to interwoven CNT [87],  $\text{MoS}_2$  decorated LIG [19], CNT- $\text{MnO}_2$ -polymer fiber [88] and Porous LIG [89], (e) Nyquist plots of experimental and fitted impedance data for prototype LIG-RM device, the red line corresponds to fitted data and (f) the glowing of a white LED using a prototype device [The inset represents the open circuit (no supercapacitor was connected)].

### 3. Conclusions

The LIG-RM supercapacitor based 2 electrodes flexible all-solid-state micro-supercapacitor with polymer ionogel was successfully fabricated. The waste red mud, an abundant source of iron oxide was decorated over the laser-induced graphene. The two-electrode cell exhibits promising and stable supercapacitor behavior. The stored charge in the supercapacitor device was dominated by intercalation governed pseudocapacitance. The device displayed significant specific capacitance along with high energy and power densities. The long-term cyclic performance at ambient condition was also promising. Bending tests confirm its suitability as a flexible device. Finally, the prototype device was able to power up a white LED. The present approach does not involve any harsh chemicals and also deals with industrial waste material, the fabrication process is inexpensive and is an encouraging route towards sustainability.

## Experimental Section

### Materials

Raw red mud was collected from National Aluminum Company Limited (NALCO), India. The polyimide sheet of 50  $\mu\text{m}$  thickness was purchased from Printed Electronics (PEL), UK. 1-Ethyl-3-methylimidazolium bis(trifluoromethylsulfonyl)imide ([EMIM][TFSI], 1-Ethyl-3-methylimidazolium tetrafluoroborate ([EMIM][BF<sub>4</sub>]) and Poly(vinylidene fluoride-co-hexafluoropropylene) (PVDF-HFP) of high purities were purchased from Sigma-Aldrich and were used without any further purification. All aqueous solutions were prepared using ultrapure de-ionized (DI) water (Millipore-Q system).

## **Synthesis of Red mud nanoparticles**

Red mud nanoparticles were synthesized from the as-received red mud powder according to the process already reported in the literature [43]. Briefly, the powders were at first dried inside an oven for 1 hour at an elevated temperature (383K) and crushed using a motor-pastel to obtain dehydrated, and homogenous microparticles. RM nanoparticles were synthesized using a planetary ball mill (Retsch, PN200) and pulverized inside a 60ml chrome steel bowl filled with RM powders and spherical steel balls (diameter 5mm). An optimum ball to RM mass ratio of 8:1 was employed and the milling was carried out at a rotation speed of 150 rpm for 10 hours.

## **Synthesis of LIG**

Kapton polyimide of 50  $\mu\text{m}$  thickness (Printed electronics ltd. UK) was used as received for the LIG production. Laser treatment was performed with a Universal Laser 230 VLS under ambient conditions. The power throughout was 8.1 W (32.5 % of the maximum of this 25 W system), speed was 570  $\text{mm s}^{-1}$  (50 % of the maximum speed of the system) and at a density of 1000 PPI. The device was fabricated as an in-plane interdigitated structure, the electrode 'fingers' were 0.5 mm wide, 2.5 mm long, and with a 0.5 mm separation between fingers. The total area was 77.25  $\text{mm}^2$  and this is used in calculations for cell capacitance

## **Synthesis of ionogel electrolyte**

In order to prepare the ionogel, the ILs [EMI][TFSI] and [EMIM][BF<sub>4</sub>] were mixed in a 3:1 ratio. Separately, PVDF-HFP was dissolved in acetone as a 1 mg/ml concentration. The RTIL solution was then mixed with the PVDF-HFP solution (3:1), heated at 50 °C and stirred to produce a homogenous mixture.

## Characterization

TEM imaging was performed using JEOL 2100F. RM nanoparticles were dispersed in methanol, sonicated until the dispersion was uniform, and micro-pipetted over a copper grid. Scanning electron microscopy was completed using a Hitachi SU5000, acceleration voltage 10kV, working distance ~6 mm. The Brunauer–Emmett–Teller (BET) analysis was employed to measure the specific surface area of LIG-RM with a Quantachrome Autosorb-1 BET surface analyzer at 77K. X-ray photoelectron spectroscopy was performed using a Kratos Axis Ultra using a monochromatic Al K $\alpha$  X-ray source ( $\hbar\nu$  1486 eV). The survey scan window was 287 to 1892 eV with a dwell time of 0.2 seconds. The 28 eV window high-resolution scans were performed in triplicate with a dwell time of 0.5 seconds. The active mass was measured by producing 252 cm<sup>2</sup> each of both LIG and LIG-RM and delaminating these from the substrate before measuring using an analytical balance. The CV, charging-discharging and EIS measurements were carried out in a 2-electrode cell configuration using an Autolab Potentiostat/ Galvanostat (PGSTAT3, Metrhom, Netherlands). The equivalent circuit elements were extracted from the Nyquist plots using the vendor-supplied Nova software.

## Acknowledgements

G.B. acknowledges the Commonwealth Split-Site Scholarship, from the Commonwealth Scholarship Commission in the UK. G.B., S.J.F., and J.A.M. are grateful for funding under the Biodevices Laboratory from Invest NI. A.P. is indebted to Shiv Nadar University for providing PhD scholarships. A.P. acknowledges Shiv Nadar University for PhD funding. We all thank National Aluminium Company Ltd. for supplying the red mud samples.

## 1 References

- 2 [1] B. Dyatkin, V. Presser, M. Heon, M. R. Lukatskaya, M. Beidaghi, Y. Gogotsi, *ChemSusChem*  
3 **2013**, 6, 2269-2280.
- 4 [2] a) X. Wang, Z. Liu, T. Zhang, *Small* **2017**, 13, 1602790; b) Y. Liu, M. Pharr, G. A. Salvatore,  
5 *ACS Nano* **2017**, 11, 9614-9635.
- 6 [3] D. P. Dubal, N. R. Chodankar, D.-H. Kim, P. Gomez-Romero, *Chemical Society Reviews* **2018**,  
7 47, 2065-2129.
- 8 [4] J. Gao, C. Shao, S. Shao, F. Wan, C. Gao, Y. Zhao, L. Jiang, L. Qu, *Small* **2018**, 14, 1801809.
- 9 [5] L. Zhang, W. Viola, T. L. Andrew, *ACS Applied Materials & Interfaces* **2018**, 10, 36834-  
10 36840.
- 11 [6] L. L. Zhang, X. S. Zhao, *Chemical Society Reviews* **2009**, 38, 2520-2531.
- 12 [7] D. V. Chernysheva, Y. A. Chus, V. A. Klushin, T. A. Lastovina, L. S. Pudova, N. V. Smirnova,  
13 O. A. Kravchenko, V. M. Chernyshev, V. P. Ananikov, *ChemSusChem* **2018**, 11, 3599-3608.
- 14 [8] M. P. Down, C. W. Foster, X. Ji, C. E. Banks, *RSC Advances* **2016**, 6, 81130-81141.
- 15 [9] R. Ye, D. K. James, J. M. Tour, *Accounts of Chemical Research* **2018**, 51, 1609-1620.
- 16 [10] J. Lin, Z. Peng, Y. Liu, F. Ruiz-Zepeda, R. Ye, E. L. G. Samuel, M. J. Yacaman, B. I. Yakobson,  
17 J. M. Tour, *Nature Communications* **2014**, 5, 5714.
- 18 [11] J. Chang, M. Jin, F. Yao, T. H. Kim, V. T. Le, H. Yue, F. Gunes, B. Li, A. Ghosh, S. Xie, Y.  
19 H. Lee, *Advanced Functional Materials* **2013**, 23, 5074-5083.
- 20 [12] a) B. E. Conway, V. Birss, J. Wojtowicz, *Journal of Power Sources* **1997**, 66, 1-14; b) X. Y.  
21 Liu, Y. Q. Gao, G. W. Yang, *Nanoscale* **2016**, 8, 4227-4235.
- 22 [13] J. W. Lee, A. S. Hall, J.-D. Kim, T. E. Mallouk, *Chemistry of Materials* **2012**, 24, 1158-1164.
- 23 [14] J. Yang, T. Lan, J. Liu, Y. Song, M. Wei, *Electrochimica Acta* **2013**, 105, 489-495.
- 24 [15] a) C. Guan, J. Liu, Y. Wang, L. Mao, Z. Fan, Z. Shen, H. Zhang, J. Wang, *ACS Nano* **2015**, 9,  
25 5198-5207; b) A. Borenstein, O. Hanna, R. Attias, S. Luski, T. Brousse, D. Aurbach, *Journal*  
26 *of Materials Chemistry A* **2017**, 5, 12653-12672.



- 1 [16] F. Clerici, M. Fontana, S. Bianco, M. Serrapede, F. Perrucci, S. Ferrero, E. Tresso, A. Lamberti,  
2 *ACS Applied Materials & Interfaces* **2016**, 8, 10459-10465.
- 3 [17] a) L. Fenghua, S. Jiangfeng, Y. Huafeng, G. Shiyu, Z. Qixian, H. Dongxue, I. Ari, N. Li,  
4 *Nanotechnology* **2009**, 20, 455602; b) H. R. Naderi, A. Sobhani-Nasab, M. Rahimi-Nasrabadi,  
5 M. R. Ganjali, *Applied Surface Science* **2017**, 423, 1025-1034.
- 6 [18] K. Turcheniuk, D. Bondarev, V. Singhal, G. Yushin, Nature Publishing Group, **2018**.
- 7 [19] a) J. B. Dunn, L. Gaines, J. C. Kelly, C. James, K. G. Gallagher, *Energy & Environmental*  
8 *Science* **2015**, 8, 158-168; b) P. Nuss, M. J. Eckelman, *PLoS One* **2014**, 9, e101298.
- 9 [20] D. A. G. Hegde, *RSC Advances* **2015**, 5, 88339-88352.
- 10 [21] C. Fu, P. S. Grant, *ACS Sustainable Chemistry & Engineering* **2015**, 3, 2831-2838.
- 11 [22] C. Fu, A. Mahadevegowda, P. S. Grant, *Journal of Materials Chemistry A* **2016**, 4, 2597-2604.
- 12 [23] a) R. Milačič, T. Zuliani, J. Ščančar, *Science of The Total Environment* **2012**, 426, 359-365; b)  
13 Z. Chen, Q. Zhang, L. Huang, R. Li, W. Li, G. Xu, H. Cheng, *The Journal of Physical Chemistry*  
14 *C* **2014**, 118, 21244-21249; c) Y. Liu, R. Naidu, H. Ming, *Geoderma* **2011**, 163, 1-12.
- 15 [24] G. Power, M. Gräfe, C. Klauber, *Hydrometallurgy* **2011**, 108, 33-45.
- 16 [25] M. K. Sahu, R. K. Patel, in *Environmental Materials and Waste* (Eds.: M. N. V. Prasad, K.  
17 Shih), Academic Press, **2016**, pp. 485-524.
- 18 [26] M. Enserink, *Science* **2010**, 330, 432-433.
- 19 [27] A. Anton, M. Rékási, N. Uzinger, G. Széplábi, A. Makó, *Water, Air, & Soil Pollution* **2012**,  
20 223, 5175-5188.
- 21 [28] S. Samal, A. K. Ray, A. Bandopadhyay, *International Journal of Mineral Processing* **2013**,  
22 118, 43-55.
- 23 [29] S. Wang, Y. Boyjoo, A. Choueib, Z. Zhu, *Water research* **2005**, 39, 129-138.
- 24 [30] V. K. Gupta, M. Gupta, S. Sharma, *Water Research* **2001**, 35, 1125-1134.
- 25 [31] A. Tor, N. Danaoglu, G. Arslan, Y. Cengeloglu, *Journal of Hazardous Materials* **2009**, 164,  
26 271-278.

- 1 [32] V. K. Gupta, I. Ali, V. K. Saini, *Environmental Science & Technology* **2004**, 38, 4012-4018.
- 2 [33] I. Akin, G. Arslan, A. Tor, M. Ersoz, Y. Cengeloglu, *Journal of Hazardous Materials* **2012**,  
3 235-236, 62-68.
- 4 [34] S. F. Kurtoğlu, A. Uzun, *Scientific Reports* **2016**, 6, 32279.
- 5 [35] A. Agrawal, K. K. Sahu, B. D. Pandey, *Resources, Conservation and Recycling* **2004**, 42, 99-  
6 120.
- 7 [36] G. Bhattacharya, S. J. Fishlock, J. S. Roy, A. Pritam, D. Banerjee, S. Deshmukh, S. Ghosh, J.  
8 A. McLaughlin, S. S. Roy, *Global Challenges* **2019**, 3, 1800066.
- 9 [37] a) A. Balducci, R. Dugas, P. L. Taberna, P. Simon, D. Plée, M. Mastragostino, S. Passerini,  
10 *Journal of Power Sources* **2007**, 165, 922-927; b) A. Lewandowski, A. Olejniczak, M. Galinski,  
11 I. Stepniak, *Journal of Power Sources* **2010**, 195, 5814-5819.
- 12 [38] C. Yuan, X. Zhang, Q. Wu, B. Gao, *Solid State Ionics* **2006**, 177, 1237-1242.
- 13 [39] S. Shahzad, A. Shah, E. Kowsari, F. J. Iftikhar, A. Nawab, B. Piro, M. S. Akhter, U. A. Rana,  
14 Y. Zou, *Global Challenges* **2018**, 0, 1800023.
- 15 [40] a) B. Xu, F. Qi, J. Zhang, H. Li, D. Sun, D. Robert, Z. Chen, *Chemical Engineering Journal*  
16 **2016**, 284, 942-952; b) J. Liu, Y. Yu, S. Zhu, J. Yang, J. Song, W. Fan, H. Yu, D. Bian, M.  
17 Huo, *PloS one* **2018**, 13, e0191229.
- 18 [41] M. R. Bobinger, F. J. Romero, A. Salinas-Castillo, M. Becherer, P. Lugli, D. P. Morales, N.  
19 Rodríguez, A. Rivadeneyra, *Carbon* **2019**, 144, 116-126.
- 20 [42] D. Majumdar, N. Baugh, S. K. Bhattacharya, *Colloids and Surfaces A: Physicochemical and*  
21 *Engineering Aspects* **2017**, 512, 158-170.
- 22 [43] a) W. Chen, Z. Fan, L. Gu, X. Bao, C. Wang, *Chemical Communications* **2010**, 46, 3905-3907;  
23 b) B. Anothumakkool, S. N. Bhange, M. V. Badiger, S. Kurungot, *Nanoscale* **2014**, 6, 5944-  
24 5952.

- 1 [44] a) P. Liu, J. Liu, S. Cheng, W. Cai, F. Yu, Y. Zhang, P. Wu, M. Liu, *Chemical Engineering*  
2 *Journal* **2017**, 328, 1-10; b) C. Wei, Y. Huang, S. Xue, X. Zhang, X. Chen, J. Yan, W. Yao,  
3 *Chemical Engineering Journal* **2017**, 317, 873-881.
- 4 [45] K. V. Sankar, R. K. Selvan, D. Meyrick, *Rsc Advances* **2015**, 5, 99959-99967.
- 5 [46] a) M. Sathiya, A. S. Prakash, K. Ramesha, J. M. Tarascon, A. K. Shukla, *Journal of the*  
6 *American Chemical Society* **2011**, 133, 16291-16299; b) Q. Xue, H. Gan, Y. Huang, M. Zhu,  
7 Z. Pei, H. Li, S. Deng, F. Liu, C. Zhi, *Advanced Energy Materials* **2018**, 8, 1703117.
- 8 [47] W. Yan, J. Y. Kim, W. Xing, K. C. Donovan, T. Ayvazian, R. M. Penner, *Chemistry of*  
9 *Materials* **2012**, 24, 2382-2390.
- 10 [48] a) K. Brezesinski, J. Wang, J. Haetge, C. Reitz, S. O. Steinmueller, S. H. Tolbert, B. M.  
11 Smarsly, B. Dunn, T. Brezesinski, *Journal of the American Chemical Society* **2010**, 132, 6982-  
12 6990; b) J. Zhou, J. Yu, L. Shi, Z. Wang, H. Liu, B. Yang, C. Li, C. Zhu, J. Xu, *Small* **2018**,  
13 14, 1803786.
- 14 [49] K. V. Sankar, R. K. Selvan, *RSC Advances* **2014**, 4, 17555-17566.
- 15 [50] a) J. Duay, S. A. Sherrill, Z. Gui, E. Gillette, S. B. Lee, *Acs Nano* **2013**, 7, 1200-1214; b) G.  
16 Kim, I. Ryu, S. Yim, *Scientific reports* **2017**, 7, 8260.
- 17 [51] J. Sun, A. Iakunkov, A. T. Rebrikova, A. V. Talyzin, *Nanoscale* **2018**, 10, 21386-21395.
- 18 [52] Q. Zhang, Z. Liu, B. Zhao, Y. Cheng, L. Zhang, H.-H. Wu, M.-S. Wang, S. Dai, K. Zhang, D.  
19 Ding, Y. Wu, M. Liu, *Energy Storage Materials* **2019**, 16, 632-645.
- 20 [53] S. Xiong, F. Yang, H. Jiang, J. Ma, X. Lu, *Electrochimica Acta* **2012**, 85, 235-242.
- 21 [54] a) D. Shan, J. Yang, W. Liu, J. Yan, Z. Fan, *Journal of Materials Chemistry A* **2016**, 4, 13589-  
22 13602; b) K. K. Upadhyay, M. Altomare, S. Eugénio, P. Schmuki, T. M. Silva, M. F.  
23 Montemor, *Electrochimica Acta* **2017**, 232, 192-201.
- 24 [55] C. Huang, J. Zhang, N. P. Young, H. J. Snaith, P. S. Grant, *Scientific Reports* **2016**, 6, 25684.
- 25 [56] D. Zhang, Q.-Q. Dong, X. Wang, W. Yan, W. Deng, L.-Y. Shi, *The Journal of Physical*  
26 *Chemistry C* **2013**, 117, 20446-20455.

- 1 [57] G. Bhattacharya, G. Kandasamy, N. Soin, R. K. Upadhyay, S. Deshmukh, D. Maity, J.  
2 McLaughlin, S. S. Roy, *RSC Advances* **2017**, 7, 327-335.
- 3 [58] G. Yu, L. Hu, N. Liu, H. Wang, M. Vosgueritchian, Y. Yang, Y. Cui, Z. Bao, *Nano letters*  
4 **2011**, 11, 4438-4442.
- 5 [59] B. G. Choi, M. Yang, W. H. Hong, J. W. Choi, Y. S. Huh, *ACS nano* **2012**, 6, 4020-4028.
- 6 [60] M. D. Stoller, R. S. Ruoff, *Energy & Environmental Science* **2010**, 3, 1294-1301.
- 7 [61] C. Zequine, C. Ranaweera, Z. Wang, S. Singh, P. Tripathi, O. Srivastava, B. K. Gupta, K.  
8 Ramasamy, P. Kahol, P. Dvornic, *Scientific reports* **2016**, 6, 31704.
- 9 [62] Q. Liu, Q. Shi, H. Wang, Q. Zhang, Y. Li, *RSC Advances* **2015**, 5, 47074-47079.
- 10 [63] X. Xia, J. Tu, Y. Zhang, X. Wang, C. Gu, X.-b. Zhao, H. J. Fan, *ACS Nano* **2012**, 6, 5531-5538.
- 11 [64] a) N. C. Osti, A. Gallegos, B. Dyatkin, J. Wu, Y. Gogotsi, E. Mamontov, *The Journal of*  
12 *Physical Chemistry C* **2018**, 122, 10476-10481; b) C. Lian, K. Liu, K. L. Van Aken, Y. Gogotsi,  
13 D. J. Wesolowski, H. Liu, D. Jiang, J. Wu, *ACS Energy Letters* **2016**, 1, 21-26.
- 14 [65] K. Rajendra Prasad, N. Miura, *Electrochemistry Communications* **2004**, 6, 1004-1008.
- 15 [66] Y. Yang, D. Kim, M. Yang, P. Schmuki, *Chemical Communications* **2011**, 47, 7746-7748.
- 16 [67] X. Li, J. Shao, S.-K. Kim, C. Yao, J. Wang, Y.-R. Miao, Q. Zheng, P. Sun, R. Zhang, P. V.  
17 Braun, *Nature Communications* **2018**, 9, 2578.
- 18 [68] a) L. Huang, D. Chen, Y. Ding, Z. L. Wang, Z. Zeng, M. Liu, *ACS applied materials &*  
19 *interfaces* **2013**, 5, 11159-11162; b) R. Liu, S. B. Lee, *Journal of the American Chemical*  
20 *Society* **2008**, 130, 2942-2943; c) C. Shang, S. Dong, S. Wang, D. Xiao, P. Han, X. Wang, L.  
21 Gu, G. Cui, *ACS Nano* **2013**, 7, 5430-5436.
- 22 [69] R. Zhang, J. Ding, C. Liu, E.-H. Yang, *ACS Applied Energy Materials* **2018**, 1, 2048-2055.
- 23 [70] C. Choi, S. H. Kim, H. J. Sim, J. A. Lee, A. Y. Choi, Y. T. Kim, X. Lepró, G. M. Spinks, R. H.  
24 Baughman, S. J. Kim, *Scientific Reports* **2015**, 5, 9387.
- 25 [71] J. Lin, Z. Peng, Y. Liu, F. Ruiz-Zepeda, R. Ye, E. L. Samuel, M. J. Yacaman, B. I. Yakobson,  
26 J. M. Tour, *Nature communications* **2014**, 5, 5714.

- [72] E. Barsoukov, J. R. Macdonald, *Impedance spectroscopy: theory, experiment, and applications*, John Wiley & Sons, **2018**.
- [73] a) G. Bhattacharya, S. Sas, S. Wadhwa, A. Mathur, J. McLaughlin, S. S. Roy, *RSC Advances* **2017**, 7, 26680-26688; b) G. Bhattacharya, K. J. Sankaran, S. B. Srivastava, J. P. Thomas, S. Deshmukh, P. Pobedinskas, S. P. Singh, K. T. Leung, M. K. Van Bael, K. Haenen, *Electrochimica Acta* **2017**, 246, 68-74.
- [74] G. Bhattacharya, A. Mathur, S. Pal, J. McLaughlin, S. S. Roy, *Int J Electrochem Sci* **2016**, 11, 6370-6386.
- [75] a) Y. Xie, Y. Liu, Y. Zhao, Y. H. Tsang, S. P. Lau, H. Huang, Y. Chai, *Journal of Materials Chemistry A* **2014**, 2, 9142-9149; b) H. Fei, N. Saha, N. Kazantseva, R. Moucka, Q. Cheng, P. Saha, *Materials* **2017**, 10, 1251.